High-resolution electron microscopy of the tweed structure associated with the FCC-FCT martensitic transformation of Fe-Pd alloys

1989 J. Phys.: Condens. Matter 1 9971

(http://iopscience.iop.org/0953-8984/1/50/001)

J. Phys.: Condens. Matter 1 (1989) 9971–9983. Printed in the UK

High-resolution electron microscopy of the tweed structure associated with the FCC–FCT martensitic transformation of Fe–Pd alloys

Shunsuke Muto†, Seiji Takeda†, Ryuichiro Oshima‡ and Francisco Eiichi Fujita‡

† Physics Department, College of General Education, Osaka University, Toyonaka, Osaka 560, Japan

‡ Department of Material Physics, Faculty of Engineering Science, Osaka University, Toyonaka, Osaka 560, Japan

Received 25 May 1989

Abstract. High-resolution electron microscopy (HREM) was performed on a modulated lattice structure (tweed structure) appearing prior to the FCC–FCT martensitic transformation of Fe–Pd alloys. The local lattice modulations of the cubic phase were quite irregularly distributed in the matrix, which supports the 'embryo model' of the tweed structure. Furthermore, the image simulation based on the model well reproduced the features observed in the high-resolution images.

1. Introduction

Precursor phenomena have been one of the most attractive concepts for many investigators of martensitic transformations in explaining their mechanisms and these have been intensively investigated since the late 1970s [1]. The types of martensitic transformation which display precursor phenomena generally belong to the group referred to as weakly-first-order phase transitions: the discontinuous entropy change at the transition point is small and thereafter the degree of order of the product phase (or the order parameter) develops continuously [2]. These types of transformation have been understood by extrapolating the scheme for continuous phase transitions, or second-order phase transitions, that is to say, the precursor phenomena correspond to the critical phenomena associated with the impending structural change [3, 4].

The tweed structure, which is one typical precursor phenomenon, appears in electron micrographs prior to cubic–tetragonal phase transitions, and is characterised by cross-hatched anomalous contrast parallel to the traces of {110} planes. The tweed contrast is always accompanied by the diffuse streaking in $\langle 110 \rangle^*$ directions§ of diffracted beams. This diffuse scattering obeys the extinction rule consistent with $\{110\}\langle 110 \rangle$ atomic shear displacements associated with a reduction of the elastic constant, $C'(=(C_{11}-C_{12})/2)$. It is natural in the above described context that the tweed structure was understood to be

§ The symbol '*' means the plane or direction indexed in reciprocal lattice space.

0953-8984/89/509971 + 13 $02.50

due to dynamical strain waves [5] or fluctuating embryos [6], reflecting the incipient symmetry change to the tetragonal phase.

However, recent electron microscopy of the tweed structure of Fe–Pd alloys [7, 8] has shown that the tweed structure can be ascribed to static displacements of atoms. The concept of critical fluctuation was therefore found to be inappropriate to explain the tweed structure. On the other hand, there have been different opinions that the tweed is a thin-foil effect [9], and partially or wholly a surface phenomenon [10]. In this respect, Tendeloo and co-workers [11] examined the tweed microstructures in β Cu–Zn–Al by means of high-resolution electron microscopy and concluded that the tweed is a subsurface phenomenon and a major part of the diffuse streaking in electron diffraction has to be attributed to thermal diffuse scattering, whereas Schryvers and co-workers [12] claimed on the basis of tweed microstructures on a Ni–Al ordered alloy that uniform periodic distortions bringing a transitional configuration to the martensite structure were consistent with the observed high-resolution images. Thus, the nature of the tweed structures is likely to depend on the alloy system.

In the tweed of the Fe–Pd alloy system, the 'embryo model' was proposed, based on detailed observations [7, 13]; small FCT platelets (a few nanometers in size) are nonuniformly but with a preferential configuration dispersed in the FCC matrix, resulting in the tweedy texture. This mixed state reduces the total free energy of the system by the amount of entropy of mixing and the transition from FCC to FCT phase exhibits a second-order-like nature as a consequence [13]. The model therefore seems to be quite successful.

The purpose of the present study is to clarify directly the atomic configuration underlying the tweed structure of Fe–Pd alloys by means of high-resolution electron microscopy. This alloy system is suitable for this purpose, because (i) the crystal structures of both phases are simple (FCC and FCT), which allows intuitive interpretation of the high-resolution images, and (ii) since the transformation temperature (M_s) varies sensitively with the alloy composition [7], the various stages leading to the FCT phase can be observed *in situ* at room temperature by changing the palladium concentration.

Furthermore, in a later section image simulation based on the embryo model is demonstrated, to discuss the entity causing the tweed structure.

2. Experimental procedure

Two types of Fe–Pd alloys containing around 30 at.% Pd were prepared. One partially transformed to the FCT phase at room temperature, whereas the other remained FCC. The M_s temperature of the latter was about 20 K below room temperature. Foils of the alloys were solution treated at 1373 K for 18 ks, and quenched into iced water. Specimens for transmission electron microscopy were made by electropolishing in a mixed solution of 82% acetic acid, 9% perchloric acid and 9% ethanol (by volume). High-resolution observation was carried out at room temperature on a JEOL JEM-4000EX electron microscope (C_s = 1.0 mm, C_c = 1.6 mm, point-to-point resolution of 0.17 nm) operated at 400 kV.

3. Experimental results

3.1. High-resolution image of the tweed structure

An ordinary bright-field image of a typical tweed contrast of the FCC phase at room temperature is shown in figure 1. This is from an Fe–30.0 at.% Pd alloy whose M_s

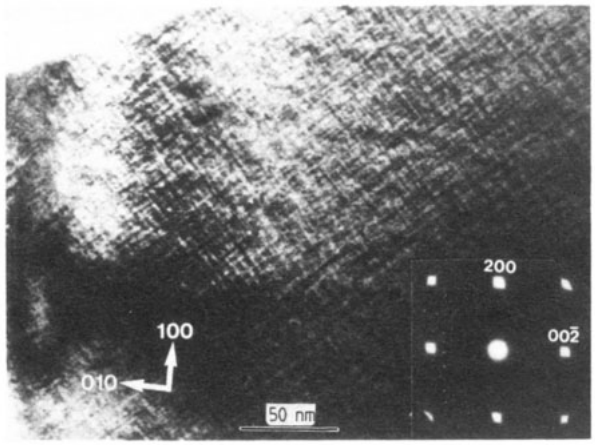

Figure 1. Bright-field image of the tweed structure in an Fe–30.0 at.% Pd alloy. Inset: electron diffraction pattern from the area.

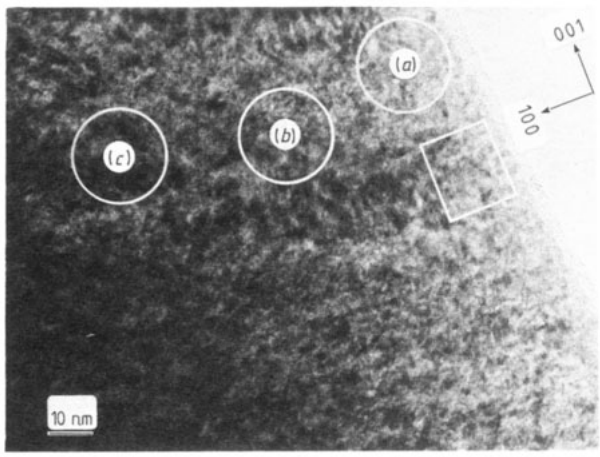

Figure 2. High-resolution electron micrograph of the tweed structure. See text for detail.

temperature is 265 K. The structure consists of the traces of the (110) and (1$\bar{1}$0) planes at intervals of a few nanometers. The inset electron diffraction pattern from the region in the figure shows the diffuse streaking perpendicular to the traces of the tweed emanating from each Bragg spot.

A low-magnification, high-resolution image from a thinner part of the specimen is shown in figure 2. We note that a dark mottled contrast covers the whole area and its density becomes greater in the thicker part of the specimen, gradually exhibiting directionality, which we considered to be connected with the tweed pattern of the bright-field image in figure 1. This suggests that the dark mottles are a consequence of some lattice modulation giving rise to the tweed contrast, and that the tweed structure is not a surface effect but is revealed by the superposition of the modulated regions arranged in a specific configuration.

Optical diffraction patterns taken from the corresponding encircled area in figure 2 are shown in figure 3. The patterns displayed the cubic 100 pattern, but the Bragg spots broaden reflecting the distorted lattice planes. Since the optical diffraction patterns were taken from small areas of the high-resolution image, the characteristics of the diffracted

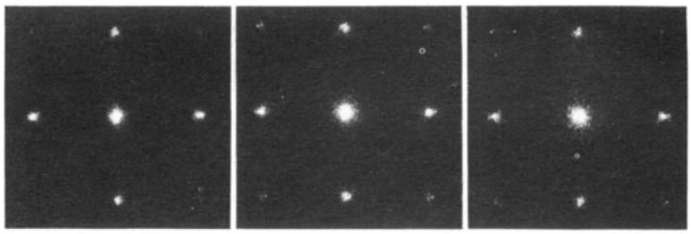

Figure 3. Optical diffraction patterns from the corresponding encircled areas (*a*), (*b*) and (*c*) in figure 2.

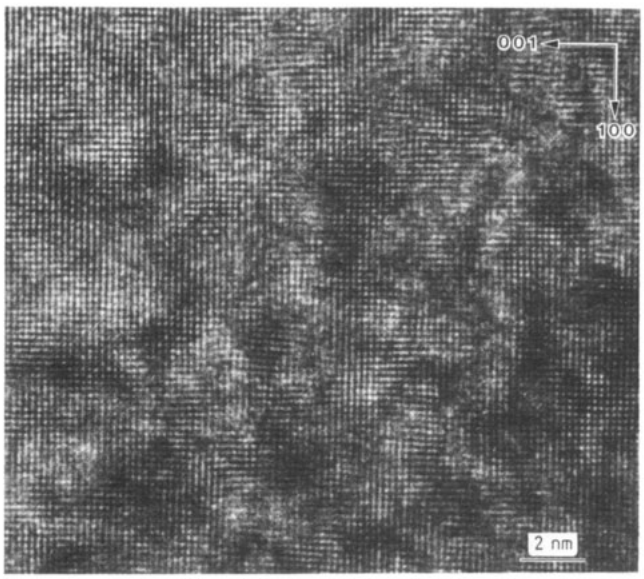

Figure 4. Enlarged image of the framed area in figure 2.

spots are ambiguous, although from the shape of the spots it can be observed qualitatively that the optical diffraction spots from a thicker region are sharper and more clearly reproduce the diffuse scattering extending in $\langle 110 \rangle^*$ directions in the electron diffraction of figure 1. This not only confirms that the lattice modulations in the micrograph which are mainly responsible for the diffuse streaking are static, but also supports the issue mentioned before that the tweed structure is caused by joining and superposing the distorted regions in the FCC matrix. Hence the high-resolution image is believed to carry the information on the lattice modulations giving rise to the tweed contrast. In this respect, it is expected that in the thinnest part of the specimen the atomic configuration caused by an isolated distorted region (FCT embryo) should be observable. This was previously suggested by the present authors in reference [8].

An enlarged image of the framed part of figure 2 is shown in figure 4. The edge of the specimen corresponds to the top of the picture. At first sight the disturbed regions are dispersed and they show no definable periodicity suggesting the shear strain waves. It is found by further observation that in such disturbed regions the image of the atomic rows perpendicular to the specimen film tend to coalesce to form line images in one of

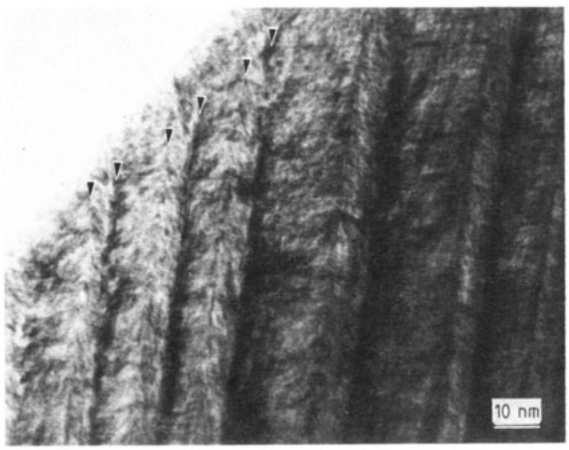

Figure 5. High-resolution electron micrograph of twinned FCT martensite. {101} twinning planes are marked by black arrowheads.

the ⟨100⟩ directions. Such slender regions extend to ⟨101⟩ directions and are surrounded by the matrix displaying the clear and regularly arranged atomic rows of the FCC lattice. This is considered to support the existence of local distorted regions (the FCT embryo platelets) lying on {101} planes in the FCC matrix. It seems, however, that the observed lattice modulations are too large for those caused by the small tetragonal distortion, so it is necessary to perform computer-simulations to discover how a localised tetragonally distorted region embedded in the FCC matrix exerts an influence on the high-resolution image, by taking into account several parameters, such as spherical aberration, amount of defocus and so forth, which will be discussed in later sections.

3.2. *FCT martensite with internal twins*

An FCT martensite phase containing internal twins was examined for comparison with the tweed structure in an FCC phase. Figure 5 is a low-magnification picture of the high-resolution image showing the [010] projection of FCT martensite into which (101) internal twins are introduced. The alternating twin boundaries which appear with bright and dark contrasts are observed at marked positions. The twin widths are 7–17 nm, which agree roughly with the average interval of the 'tweedy' striations of the cubic phase. The detailed character of the twin boundaries is revealed in the enlarged picture (figure 6). The lattice image is clearly visible at the bright twin boundaries, whereas it is obscure at the dark boundaries. One possible interpretation of this is that the types of twin boundaries in dark and bright boundaries are different. When two tetragonal lattices in a twin orientation fit together on a (101) plane, the step in the boundary can be described by the twinning dislocation [14]. When the step is parallel to [010], the twinning dislocation is of edge type; when parallel to $[10\bar{1}]$ it is of screw type. In the latter case, an array of screw dislocations produces a long-range shear of the lattice in successive (101) planes, which will result in broad and disturbed images of twin boundaries. Nevertheless, the reason why the two types of boundaries alternate as in figure 5 remains unclear.

The observed lattice planes seem to be coherently connected with each other across the twin boundaries. The tetragonality, c/a, of the FCT phase was estimated as 0.89 from the image, in agreement with that estimated from the spot splitting in the inset optical diffraction pattern. It should be noted that the atomic planes in each twin crystal are

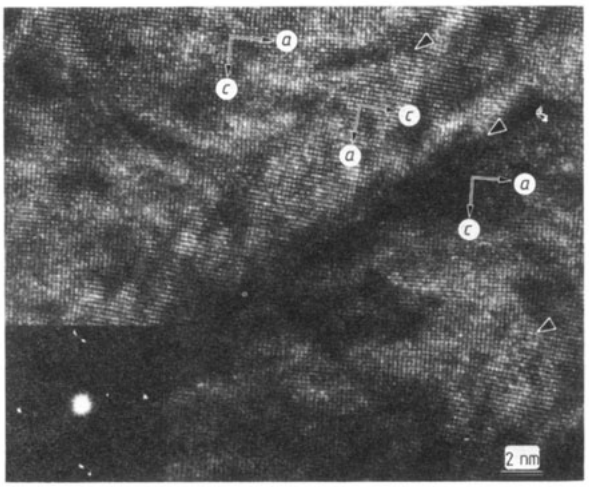

Figure 6. Enlarged image of figure 5. Inset: optical diffraction pattern from the picture.

rather regularly arranged and no considerable modulation is observed, which is also confirmed by the sharpness of the spots in the optical diffraction pattern. This supports the variant-mosaic-structure model proposed by Sugiyama for the transformation mechanism [7]. An FCT martensite variant initially consists of small FCT platelets with an identical tetragonal axis, tilted with each other, and with the increase of the tetragonality of the platelets they successively coalesce to form internal twins for the sake of the strain relaxation. Actually, the observations showed [7] that at the early stage of the transformation twin platelets seem to be formed by coalescence of the tweed debris exactly along one of the traces of the tweed structure and in the twin platelets no tweed strain contrast is observed.

The mottled-type contrast is also observed in figure 6. This suggests that small lattice modulations remain in the twin plates, even though the observed lattice planes are fairly regularly arranged. Such modulations are considered to remain in joining planes when the tetragonal platelets coalesce into twins.

4. Image simulation

4.1. Computation procedure

The computation was based on the multi-slice formulation of Cowley and Moodie [15]. Multi-slice calculations were carried out by using a practical technique developed by Ishizuka and Uyeda [16] where the convolution integrals are carried out through Fourier transforms on the basis of the Fourier theorem of convolution.

The diffraction amplitude of the electron propagating in the z direction is given by

$$\Psi_{n+1}(u, v) = \mathcal{F}\{\varphi_{n+1}(x, y)\}, \tag{1}$$

where φ_{n+1} is the wave function for the nth slice, the symbol $\mathcal{F}$ stands for the Fourier transformation, and u and v are the coordinates in reciprocal space.

The resulting intensity distribution in the image plane through the lens system is expressed by

$$I(x, y) = \mathcal{F}^{-1}\left\{\int T(\boldsymbol{u} + \boldsymbol{u}', \boldsymbol{u}')\Psi_{n+1}(\boldsymbol{u} + \boldsymbol{u}')\Psi^{*}_{n+1}(\boldsymbol{u}')\,\mathrm{d}\boldsymbol{u}'\right\}, \tag{2}$$

where $\boldsymbol{u} = (u, v)$ and $T(\boldsymbol{u} + \boldsymbol{u}', \boldsymbol{u})$ is termed a transmission cross-coefficient, which is a complex function whose value is changed by the defocus value, Δf, the spherical aberration, C_s, the defocus spread caused by chromatic aberration, Δ, and the beam divergence, α [17].

In the case where the scattering amplitudes of the diffracted beams are small compared with the transmitted beams, the contribution of the lens system to the phase contrast may be expressed as:

$$\Delta I(x, y) = \mathcal{F}^{-1}\{2\Psi_{n+1} \sin \chi\, E_{ch} \cdot E_{bc}\}. \tag{3}$$

Here

$$\chi(u, v) = \tfrac{1}{2}\pi[C_s\lambda^3(u^2 + v^2)^2 + \Delta f 2\lambda(u^2 + v^2)], \tag{4}$$

$$E_{ch}(\boldsymbol{u}) = \exp(-\tfrac{1}{2}\pi^2\lambda^2\Delta^2u^4) \tag{5}$$

and

$$E_{bc}(\boldsymbol{u}) = \exp[-\pi^2u_s^2(C_s\lambda^3u^3 - \Delta f\lambda u)^2] \tag{6}$$

where

$$u_s = \alpha/\lambda. \tag{7}$$

E_{ch} and E_{bc} are termed envelope functions, representing the effects of the chromatic aberration and the beam divergence, respectively.

4.2. Model structure used for the image simulation

The atomic positions in the unit structure for image simulation containing an embryo were determined by the continuum theory of elasticity [18]. A schematic showing of the crystal for the multi-slice iterative calculation is given in figure 7. The 'crystal' includes the region containing an FCT embryo, interposed between regions of perfect FCC crystal. The atomic displacements associated with the embryo were calculated within the confined region shown by the shaded area in the figure. The thickness of a slice was taken to be 0.375 nm which is equal to the lattice parameter of the FCC phase. An example of the calculated atomic positions of a slice projected to a (010) plane is shown in figure 8 as a unit cell for the simulation. The shape of the embryo was assumed to be an oblate spheroid with aspect ratio of 0.25 and axial ratio, c/a, of 0.92 and is delineated by the broken line in the figure. The tetragonal axis (c axis) of the embryo was taken to be parallel to the [001] axis of the cubic coordinates. To save calculation time and cost the estimation of the atom displacements associated with the embryo was confined within the area framed by the chain curve in the figure. This can be justified by the fact that the atom displacements from the FCC sites were too small at the boundary of the framed area to affect the computed image. The rest of the cell was filled with the perfect FCC crystal and was surrounded by a vacuum in the outermost part to minimise interference between neighbouring cells.

The cell edge was divided into 256 points for sampling points of the kinematic structure-factor calculation. As a result, 42473 Fourier coefficients were used to generate

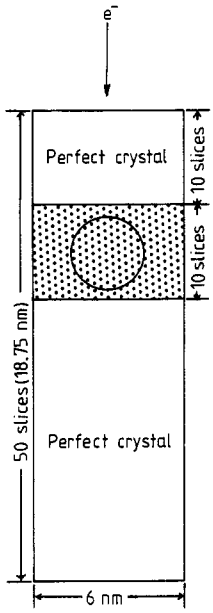

Figure 7. Cross-section of the unit structure for the multi-slice calculation in the plane parallel to the incident electron direction, based on the embryo model. The circle represents the FCT embryo and the lattice distortions associated with it were calculated within the shaded area.

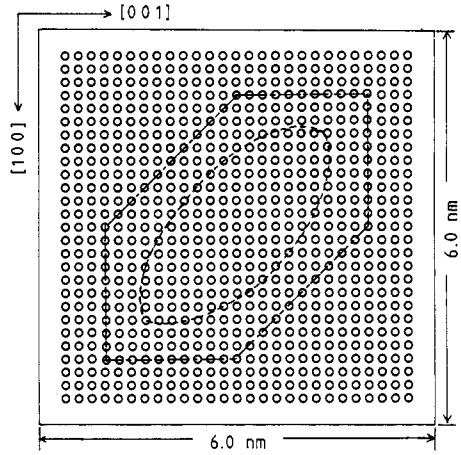

Figure 8. An example of atom positions of a unit slice containing the embryo. The shaded circles represent atomic positions. The shape of the embryo is delineated by the broken curve and the atomic displacements from the perfect FCC sites were calculated within the framed area indicated by the chain curve.

the phase-grating for each slice and 7385 beams were used for the iterative multi-slice calculations. The calculated scattering amplitudes below every slice were stored in an output file, the values of which were used for the imaging processes at an arbitrary thickness.

The set of imaging conditions which was used for the simulation is listed below:

(i) An incident electron energy of 400 keV was used.

(ii) An objective aperture picked up transmitted diffracted beams up to a maximum scattering angle given by $2(\sin\theta)/\lambda = 8.3\ \mathrm{nm}^{-1}$.

(iii) The spherical aberration constant of the microscope was estimated to be 1.0 mm (from the manufacturer's data).

(iv) The objective lens was underfocused by 0 to 80 nm from the Gaussian focus plane.

(v) The incident beam divergence was not taken into consideration in the present calculation.

This time the envelope functions introduced in (3)–(7) were used in the imaging process instead of using the exact expression of (2), as there was little difference in the resulting images from the two procedures in the case of a perfect FCC lattice. The final computed images were displayed on a cathode-ray tube with 16 steps of contrast from black to white.

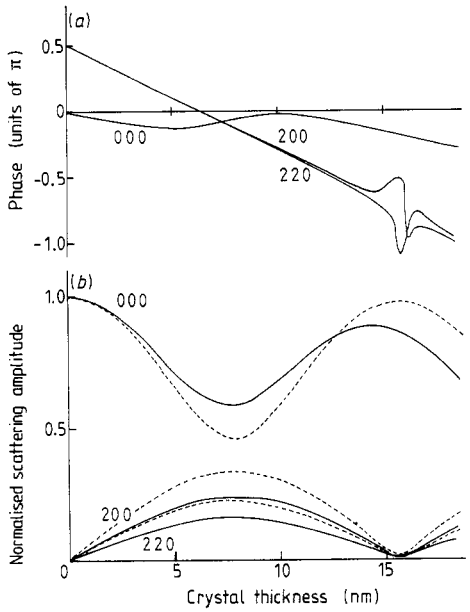

Figure 9. (*a*) Phase; and (*b*) normalised scattering amplitudes of the primary reflections as a function of crystal thickness. The full curves represent the case containing the embryo and the broken curves that of the perfect FCC lattice.

4.3. The results of computation

4.3.1. Variation of the scattering amplitude and phase with crystal thickness. The diffracted-beam amplitudes and phases for some primary reflections, calculated by the multi-slice formulation up to 18.8 nm (50 slices), are shown in figure 9. The broken lines correspond to those of the perfect FCC lattice of an Fe–30.0 at.% Pd alloy. It is seen that the scattering amplitudes oscillate with crystal thickness. Since relatively thicker specimens were examined in the present study to avoid bending of the specimen edges by the magnetic field of the objective lens pole-piece, the good high-resolution images in the previous section are therefore considered to have been taken from regions of around 15 nm thickness where the amplitude of the transmitted beam through the objective aperture restores. This will be confirmed later.

A calculated intensity distribution (diffraction pattern) of the 15 nm thick specimen in the reciprocal plane, contributing to the image formation, is shown in figure 10. The long striations extending to $\langle 100\rangle^*$ directions are due to the dimension of the unit cell for the computation (the shape factor of the square cell). It is noted that diffuse scatterings emanating from each Bragg spot in the $[10\bar{1}]^*$ direction are observed besides the $\langle 100\rangle^*$ streaks. This effect results from both the tetragonal distortion and the shape factor associated with the embryo. The direction of the diffuse streaking corresponds to that of the smaller principal axis of the embryo. In reality, there are four types of $\{110\}$ planes on which the embryos lie and hence the superposition of the contribution from each embryo will give rise to the $\langle 110\rangle^*$ diffuse streaking in actual diffraction patterns taken from the tweed structure, as in figure 1.

4.3.2. Computed images. The changes in simulated images with the amount of defocus at the specimen thickness of 15 nm are shown in figure 11. The upper row of the figure corresponds to the images of the perfect crystal without a distorted region and the lower row to those of the crystal containing an embryo. The outermost part of each image,

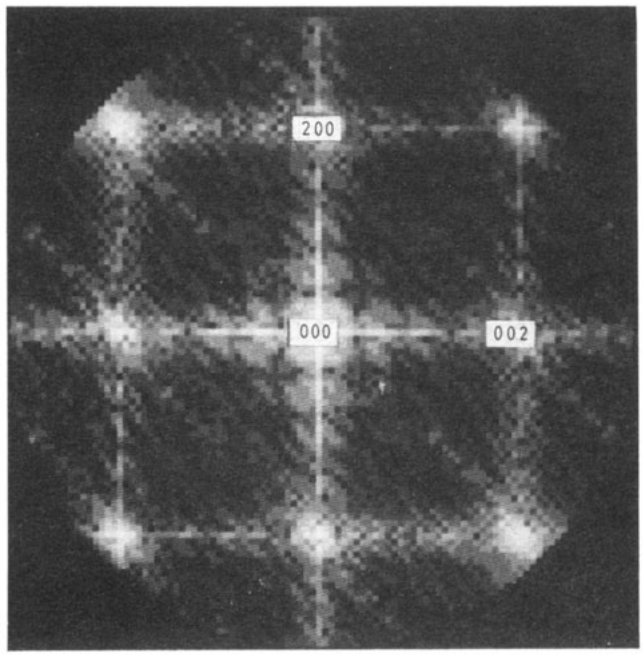

Figure 10. Calculated intensity distribution of the reflections through the objective aperture, contributing to the image formation.

showing an anomalous pattern is due to an edge effect caused by diffraction at the edge part of the unit structure used in the present simulation. The images of the perfect crystal region outside the embryo in the lower row agree well with those of the above except for the contrast, the differences of which are not essential but are due to the graphic display procedure. It is seen that the lattice distortions associated with the embryo affect the simulated images near the unit cell edges in the direction of the longer dimension of the embryo, which indicates that the unit cell size for the simulation is still insufficient in that direction. However, the essential character is well represented, as will be seen below.

On the other hand, the lower figures clearly show that the image contrast of the disturbed region associated with the tetragonally distorted region differs from that of the surrounding perfect FCC matrix; the image contrast is enhanced in the region of the embryo relative to that of the surrounding matrix. This effect was actually observed as the dispersed dark mottles, as mentioned in § 3.2. Also, comparing the computed images with the atomic configuration used for the computation in figure 8, the lattice modulation in the former is considerably exaggerated or highly disturbed like the actually observed HREM image, especially around the embryo periphery, and there is an appreciable tendency for the bright dots around the disturbed region to connect with each other making vertical lines, which is also seen in the actual HREM image. Furthermore, in the 20 nm underfocused image even dislocation-like patterns are introduced at the edge parts of the embryo as an artifact of the imaging process.

In figure 12 a series of computed micrographs at 40 nm underfocused (near the Scherzer focus) are shown, varying the thickness of the perfect crystal below the embryo

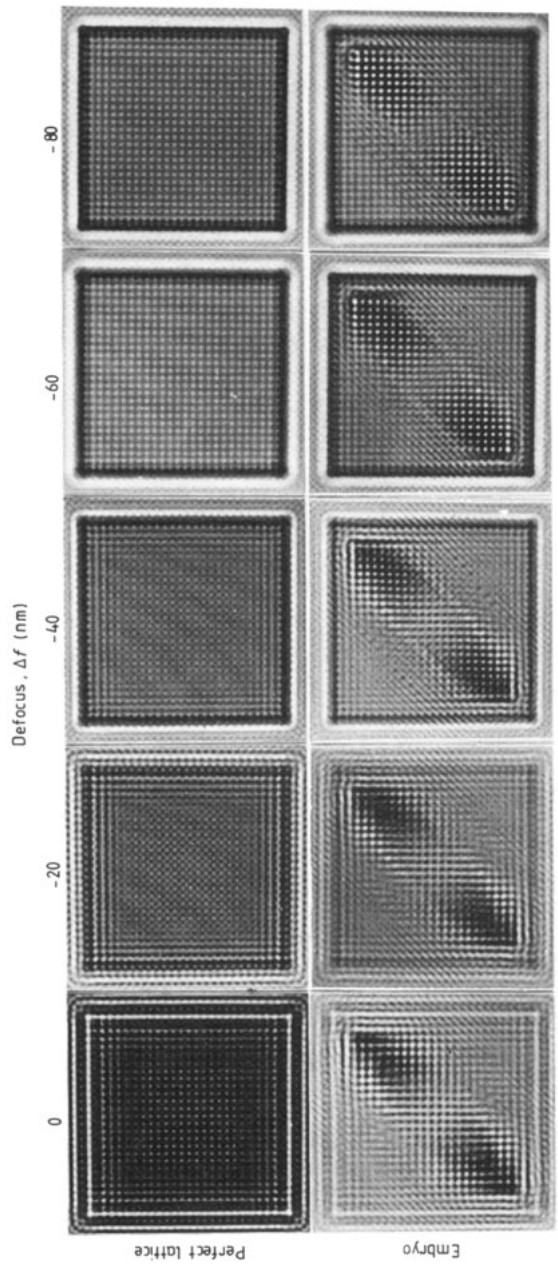

Figure 11. Simulated image s of the 15 nm thick crystals with the defo us alue varied. The ima es of the pper row are of the pe fe t FCC cry tal ind those of the lower row are of the crystal :ontaining an FCT embryo.

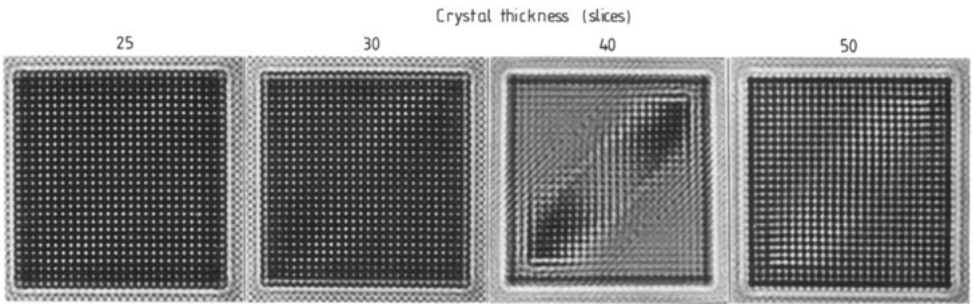

Figure 12. Change in simulated images of the crystal containing the FCT embryo with crystal thickness (underfocus $\Delta f = -40\,nm$).

(figure 7). The change in contrast of the computed images depends sensitively on the crystal thickness. As mentioned in § 4.3.1, in the thin crystals (of thickness less than 11 nm) no significant lattice distortion associated with the embryo is observed at all, because the scattering amplitude of the transmitted beam is remarkably attenuated in such regions.

5. Discussion

From the results of the high-resolution image and the image simulation it is possible to discuss to some degree the entity causing the tweed structure of Fe–Pd alloys. According to the simulated images, the embryo region exhibits clearer contrast than that of surrounding FCC matrix and the bending of lattice planes is most conspicuous around the periphery of the embryo. Moreover, images at the centre part of the embryo are too disturbed to trace the lattice planes across the region with the atomic rows connected to the neighbouring ones. Re-examining the image of figure 4 with the above features in mind, one can see the case for the disturbed regions. However, it is hard to delineate the precise shape of the embryos in figure 4 because their shape would in reality be irregular and the lattice strains must interfere with one another. Nevertheless, we consider that the dark mottled regions correspond to the embryos and hence the approximate size of an embryo can be estimated to be about 3 to 8 nm. This value is reasonable compared with the width of the tweed contrast of a bright field image, taking the range affected by the strain field associated with embryos into account.

Since the lattice modulations in figure 4 seem to cover the whole area, the density of the embryos is considered rather high at temperatures which are 20 or 30 degrees higher than the M_s. Meanwhile, in the specimen whose M_s temperature is much lower, the lattice modulations observed were less conspicuous, probably because the embryo density is lower or their tetragonality is smaller.

6. Conclusions

The results of the present study are summarised as follows:

(i) It was confirmed that the tweed structure was not a surface phenomenon but was caused by the superposition of static lattice modulations.

(ii) The lattice modulations revealed in the high-resolution electron micrographs are likely to be locally dispersed and showed no definable periodicity.

(iii) The twin boundaries in the FCT martensite were coherently connected with each other and in the twin plates lattice modulations were not observed, which supports the transformation mechanism proposed by Sugiyama and co-workers [7].

(iv) The image simulation based on the embryo model of the tweed structure reproduced the actual observed features in the high-resolution images well.

Acknowledgments

We wish to thank Mr K Ibe of JEOL Ltd for his cooperation in this high-resolution work. This work was partly supported by a Grant-in-Aid for Scientific Research from Ministry of Education, Science and Culture, Japan.

References

[1] *Proc. Int. Symp. New Aspects of Martensitic Transformations* (Tokyo: Japan Institute of Metals), Kobe 1976
[2] Delaey L, Gobin P F, Guenin G and Warlimont H 1979 *Proc. Int. Conf. Martensitic Transformations, ICOMAT-79, MIT, Cambridge, MA* p 400
[3] Murakami Y 1975 *J. Phys. Soc. Japan* **38** 404
[4] Murao T 1985 *J. Phys. Soc. Japan* **54** 2620
[5] Barsch G R and Krumhansl J A 1988 *Metall. Trans.* A **19** 761
[6] Yamada Y 1988 *Metall. Trans.* A **19** 777
[7] Sugiyama M, Oshima R and Fujita F E 1986 *Trans. Japan Inst. Met.* **27** 719
[8] Muto S, Takeda S, Oshima R and Fujita F E 1988 *Japan. J. Appl. Phys.* **27** L1387
[9] Stobbs W M 1979 *Proc. Int. Conf. Martensitic Transformations, ICOMAT-79, MIT, Cambridge, MA* p 526
[10] Robertson I M and Wayman C M 1984 *Metall. Trans.* A **15** 269
[11] Van Tendeloo G, Chandrasekaran M and Lovey F C 1986 *Metall. Trans.* A **17** 2153
[12] Schryvers D, Tanner L E and Shapiro S M 1988 *Proc. Mater. Res. Soc. Symp. Shape Memory Materials, Tokyo*, at press
[13] Fujita F E 1988 *Workshop on First-Order Displacive Phase Transformations, Oakland, CA (Mater. Sci. Eng.)*, at press
[14] Basinski Z S and Christian J W 1954 *Acta Metall.* **2** 101
[15] Cowley J M and Moodie A F 1957 *Acta Crystallogr.* **10** 609
[16] Ishizuka K and Uyeda N 1977 *Acta Crystallogr.* A **33** 740
[17] Ishizuka K 1980 *Ultramicroscopy* **5** 55
[18] Muto S, Oshima R and Fujita F E 1989 *Acta Metall.* to be published